Heriot-Watt University
Research Gateway

# Investigating the effective permeability evolution as a function of hydrate saturation in the hydrate-bearing sands using a kinetic-theory-based pore network model

**Citation for published version:**
Zhang, Y, Li, C, Ma, J, Liu, L, Golsanami, N, Wan, Y & Liu, C 2022, 'Investigating the effective permeability evolution as a function of hydrate saturation in the hydrate-bearing sands using a kinetic-theory-based pore network model', *Computers and Geotechnics*, vol. 150, 104930.
https://doi.org/10.1016/j.compgeo.2022.104930

**Digital Object Identifier (DOI):**
10.1016/j.compgeo.2022.104930

**Link:**
Link to publication record in Heriot-Watt Research Portal

**Document Version:**
Peer reviewed version

**Published In:**
Computers and Geotechnics

**Publisher Rights Statement:**
© 2022 Elsevier Ltd.

**General rights**
Copyright for the publications made accessible via Heriot-Watt Research Portal is retained by the author(s) and / or other copyright owners and it is a condition of accessing these publications that users recognise and abide by the legal requirements associated with these rights.

**Take down policy**
Heriot-Watt University has made every reasonable effort to ensure that the content in Heriot-Watt Research Portal complies with UK legislation. If you believe that the public display of this file breaches copyright please contact open.access@hw.ac.uk providing details, and we will remove access to the work immediately and investigate your claim.

Download date: 20. Jul. 2025

# Investigating the effective permeability evolution as a function of hydrate saturation in the hydrate-bearing sands using a kinetic-theory-based pore network model

Yongchao Zhang[1, 2], Chengfeng Li[1, 2*], Jingsheng Ma[3], Lele Liu[1, 2], Naser Golsanami[4], Yizhao Wan[1, 2], and Changling Liu[1, 2*]

[1] The Key Laboratory of Gas Hydrate, Ministry of Natural Resources, Qingdao Institute of Marine Geology, Qingdao 266237, China

[2] Laboratory for Marine Mineral Resources, Pilot National Laboratory for Marine Science and Technology, Qingdao 266237, China

[3] Institute of Petroleum Engineering, Heriot-Watt University, Edinburgh EH14 4AS, UK

[4] College of Mining and Safety Engineering, Shandong University of Science and Technology, Qingdao, 266590, China

* Corresponding authors:

chengfenglee@163.com (Chengfeng Li); qdliuchangling@163.com (Changling Liu)

**Abstract:**

Permeability governs the fluid flow of hydrate-bearing sediment and affects the efficiency of natural gas production from hydrate reservoirs. The permeability in hydrate-bearings sediments is estimated empirically and appears to vary widely for sediments. This study focused on the sandy hydrate-bearing sediments and intended to elucidate the evolution of effective permeability by the mean of pore network modeling. A hydrate kinetics theory-based pore network model (KT-PNM) has been developed, in which the simulation of hydrate formation in porous media is implemented by employing two sub-processes, i.e., hydrate nucleation and hydrate growth. This KT-PNM has been applied to simulate hydrate formation in different pore networks. The permeability reduction exponent ($N$) for sandy hydrate-bearing sediments is determined to fall in the range of 3 – 4 based on the simulations of seven sandy samples. An empirical equation used for predicting the effective permeability in sandy hydrate-bearing sediments has been further proposed. The developed model and simulations are hoped to provide valuable insights of pore-space effects on hydrate into permeability prediction for studying the fluid seepage in hydrate-bearing sediments and facilitate the numerical simulation of gas production from the hydrate reservoirs.

**Keywords**: natural gas hydrate; hydrate formation; pore network modeling; hydrate saturation; effective permeability; permeability reduction exponent

## 1. Introduction

Natural gas hydrates (NGHs) are ice-like crystalline solids form under low-temperature and high-pressure conditions when water molecules form a cage-like structure and trap a large number of methane gas molecules within (Boswell and Collett, 2011; Waite et al., 2009). NGHs have been regarded as an important potential source of energy because of their wide distribution in nature, a huge amount of natural gas stored, and high energy density (Boswell et al., 2020; Yin et al., 2019). Aiming at gas recovery from the hydrate-bearing sediments (HBSs), four production methods including the depressurization method, thermal simulation method, chemical inhibitor method, and gas-exchange method (Cui et al., 2018; L. Yang et al., 2019) have been proposed. Among these methods, the depressurization method is considered to be the most economically feasible technique for development of hydrate resources, which was successfully used in the hydrate production tests conducted in the Nankai Trough, Japan in 2013 and 2017 (Tamaki et al., 2017; Yamamoto et al., 2014) and the Shenhu Area of the South China Sea, China in 2017 and 2020 (Li et al., 2018; Ye et al., 2020).

Permeability is a critical parameter governing the fluid flow and affecting the mass and heat transfer processes through HBS (Cai et al., 2020; Dai and Seol, 2014; Ren et al., 2020). In the natural hydrate-bearing system, permeability impacts the methane flux to the ocean (Reagan and Moridis, 2007), methane migration and distribution (Ruppel and Kessler, 2017), hydrate concentration and accumulation (Liu and Flemings, 2007), and the efficiency of gas production from the hydrate reservoirs (Moridis et al., 2011).

In addition, permeability can be incorporated into the basin- and reservoir-scale numerical simulations for estimating resource in place and its ultimate gas recovery from hydrate reservoirs (Gupta et al., 2015; Wan et al., 2022; Wu et al., 2021). As in the conventional oil or gas reservoir, the same three types of permeability are defined in HBS including absolute permeability, effective permeability, and relative permeability, but are not referred to as inconsistent as in the former (Dai and Seol, 2014; Kumar et al., 2010; Mahabadi et al., 2016). For clarity, the absolute permeability mentioned in this work defines the ability of a single-phase-fluid to flow without the presence of hydrate; effective permeability means the single-phase-fluid permeability in the presence of solid hydrate phase; and relative permeability describes the ability of one fluid to flow in the presence of one or more other fluids. Experimental results and two-phase flow mechanisms of relative permeability in HBS are rarely revealed in literature (Moridis et al., 2019; Xu et al., 2017). Most recent studies have focused on predictions of effective permeability in HBS by means of theoretical means, experimental measurements, or the combinations, under a respective condition of hydrate formation or dissociation. Predicting effective permeability for hydrate formation is of concern in this work. For this, the term 'permeability' is used exchangeable to effective permeability unless stated otherwise.

The analytical or empirical models used for predicting the effective permeability as a function of hydrate saturation include the Tokyo model (Masuda, 1999), Kleinberg model (Kleinberg, 1999), a hybrid model (Delli and Grozic, 2013), a model proposed

by Dai and Seol (2014), and several models obtained from fractal calculations (Liu et al., 2019, 2020). In these models, the Tokyo model is most widely used because of its simple formula shown in Eq. (1).

$$K_e = (1 - S_h)^N \tag{1}$$

The Tokyo model employs the permeability reduction exponent $N$ to relate the normalized effective permeability, the ratio of effective over absolute permeability, denoted as $K_e$ to hydrate saturation $S_h$. $N$ = 10 or $N$ = 15 is given by Masuda to predict the effective permeability as a function of hydrate saturation, but no rationale is given for these specific choices. Minagawa et al. (2008) proposed a $N$ value range of 2.6 – 14 to fit the experimental data of different samples. Other reported values of $N$ in the literature range from $N$ = 3 – 5 in Kumar et al. (2010), $N$ = 3.22 in Mahabadi et al. (2019), $N$ = 4.4 in Konno et al. (2010), to $N$ = 7.7 – 9.4 in Konno et al. (2013). However, the determination of $N$ still lacks a sound physical foundation and cannot be estimated based on the petrophysical property of the host sediment (Dai and Seol, 2014). Physical experiments of permeability measurement are important for validating the above theoretical models and determining the value of $N$ in Tokyo model. However, obtaining the permeability of HBS accurately by means of experiments is challenging under the existing technical conditions. Permeability of natural hydrate-bearing samples is known as hard to be measured under in-situ conditions due to the difficulties in preserving and transporting natural samples (Waite et al., 2008). Most published experiments are completed by using artificially synthesized samples (Lei and

Santamarina, 2018; Waite et al., 2009). In the laboratory, the main challenge in measuring the permeability of artificially synthesized samples is maintaining the phase-equilibrium condition of hydrate, which should be able to prevent hydrate dissociation or reformation while preventing the formation of ice converted from water. During the measurements, injection of fluids induces temperature and pressure variations in the surrounding hydrate. Meanwhile, the pore structures of unconsolidated samples might be destroyed by the reaction of hydrate or injection of fluids. Due to these difficulties, the reported permeability data in literature from various experimental methods, specimen types, and testing conditions are widely scattered and hard to implement for further comparative analysis.

X-ray computed tomography (X-CT) imaging technology offers a route to obtain the pore-structure characteristics of the hydrate-bearing sediment (Lei et al., 2018; Zhang et al., 2021a), which facilitates the permeability prediction based on realistic CT images using numerical simulation method. Based on the high-resolution gray-scale images obtained from CT imaging, pore network modeling (PNM) is able to resemble the geometric and topologic characteristics of pore spaces by considering the pore spaces as geometrical elements composed of pores that are connected through throats (Blunt, 2001; Ma et al., 2014; Y. Yang et al., 2019) and further predict macroscopic transport properties in porous media (Chen et al., 2018; Sun et al., 2021; Wang et al., 2015), which has been one of the most widely used numerical methods in studying the HBS (Ai et al., 2017; Golsanami et al., 2022; Wang et al., 2015, 2020; Zhang et al.,

2020). Two simulation strategies for studying the permeability of HBS have been used in the literature. One is to reconstruct a series of pore networks with CT images scanned from the same hydrate-bearing sample with different hydrate saturation, then calculate the permeability of fluids through conventional PNM routes (Ai et al., 2017; Kou et al., 2021; Wang et al., 2015, 2018; Zhang et al., 2020). In this scenario, hydrates are considered as a part of the solid sediment, and the topologic characteristics of the constructed pore networks are closer to the realistic conditions of HBS. However, the accuracy of the simulation results obtained in this approach depends on the quality of CT images (Chen and Espinoza, 2018; Zhang et al., 2021b); and comparative analyses of permeability still need massive CT experimental results. Another strategy is to directly simulate the formation or/and dissociation process of hydrate in the stochastically-generated regular networks or constructed networks with CT images, then calculate the permeability as a function of hydrate saturation. The accuracy of the simulation conducted by this strategy depends on the hypotheses assumed for constraining the hydrate formation/dissociation. Mahabadi et al. (2016) extracted three-dimensional (3-D) pore networks from CT images of sediments recovered from the hydrate deposit at the Mallik site using the maximal ball algorithm (Silin and Patzek, 2006). Hydrates with various saturation and morphology were realized by assigning hydrates to fill in randomly chosen pores in patchy formations of different sizes, occupying 4, 64, or 1024 pores. Simulations conducted by Mahabadi et al. were used to study the water retention curve and permeability of HBS influenced by the hydrate

saturation and distribution morphology. Dai and Seol (2014) employed a 50×50 two-dimensional (2-D) lattice pore network to study the relationship between effective permeability and hydrate saturation. The hydrate formation process was simulated under the five conditions assumed preferential for hydrate accumulation. Given the simulation results showing the relationships between hydrate saturation and sediment porosity, and hydraulic tortuosity, they proposed a modified Kozeny-Carman model to characterize the effective permeability in HBSs. For accurate permeability prediction in the hydrate-bearing sediment, comparative analyses based on a large number of results under different conditions are essentially necessary. In this case, the second strategy mentioned above is more accessible to implement than the first one for the sake of cost. By comparing these two strategies, we can find that the hydrate formation process in porous media has not been clearly described with solid physical foundations in the previous PNM simulations. The simulation results obtained from the currently used stochastical method may cause deviations of the predicted permeability from the real tests.

We developed a PNM based on the hydrate kinetic theory (called KT-PNM) in this work. KT-PNM simulates the hydrate formation in the water-filled pore spaces by implementing the hydrate nucleation and growth process. And the simulation of single-phase fluid transport in the hydrate-bearing networks is subject to the quasi-static process. This model is applied to realistic pore-space models to analyze the relationship between hydrate saturation and effective permeability. Moreover, this work selectively

focuses on sandy HBS since the experimental results of effective permeability in sandy HBS are relatively reliable in literature and the hydrate resources with high quality mainly reside in natural sandy sediments (Li et al., 2021; Waite et al., 2009). The authors believe that the contribution of the present study to the industry is that the proposed approach lays the foundation for bridging the technical gap between the recent theoretical simulation achievements and the real natural conditions of hydrate-bearing sediments. Such an issue is further highlighted when one considers that the worldwide distributed hydrate resources occur in intrinsically different types of sediments, and thus calibrating the theoretical findings to the real reservoir situation is essential for obtaining reliable reservoir engineering results.

## 2. Hydrate formation PNM based on the kinetic theory

### 2.1 The kinetic process of hydrate formation in porous media

Hydrate formation is a time-dependent crystallization process that includes two cohesive stages: hydrate nucleation and hydrate growth, as documented by the former studies (Englezos et al., 1987; Kvamme, 2021; Sloan Jr and Koh, 2007). Hydrate nucleation is the process in which small hydrate crystals (nuclei) grow and disperse in an attempt to achieve the critical size ensuring subsequent growth (Sloan Jr and Koh, 2007). The critical size of nucleation for NGH is around 10 nanometers. In natural sediments, hydrate nucleation is influenced by many factors, including the impurities in the pore fluids (e.g., clays, nanobubbles, and microorganisms), temperature, pressure, and previously dissociated hydrate structures. Thus the quantity, occurring location, and

induction time for hydrate nucleation are usually considered stochastic with limited predictability (Sloan Jr and Koh, 2007; You et al., 2019). Hydrate growth follows the nucleation referring to the subsequent growth of nucleated hydrate crystals. The stable hydrate nuclei first grow inside the pore space in the coarse-grained sediment. Owing to the Ostwald-ripening effect (Myerson, 2002), dispersed hydrate particles in the pore are concentrated into fewer but larger particles. This process develops but is limited by accessible pore space in sediments and influenced by induced physiochemical processes by this pore confinement. Subsequently, hydrate invades the connected pores and continues to the further growth of hydrate. The process is influenced by the pore size, pore connectivity, and local effective stress (Dai et al., 2012).

The formation process of bulk hydrate in the absence of pore space confinement can be modeled using the classic van der Waals-Platteeuw (vdW-P) model (Van der Waals and Platteeuw, 1959) for predicting the thermodynamic formation condition of bulk hydrate. Clarke et al. (1999) extended the vdW-P model to predict the hydrate formation condition in porous media by adding the influence of water activity, a measure of water that is available to react with another material (Azimi et al., 2021). They expressed the water activity ($a_w$) in porous media as a function of pore radius ($r$), contact angle of the mineral surface ($\theta$), surrounding temperature ($T$), interfacial tension between mineral and water ($\sigma$), and the volume of water in the pore ($V$), as shown in Eq. (2). By using the conception of water activity, the influence of sedimentary property on the hydrate formation in the porous media can be described

and predicted.

$$a_w = EXP\left(-\frac{2\sigma V}{rRT}\cos\theta\right) \tag{2}$$

## 2.2 Model hypotheses and simulation procedure

Applications of using water activity in predicting the hydrate formation in porous media have been proved feasible in many previous thermodynamic works (Azimi et al., 2021; Chen et al., 2010). Chen et al. (2010) developed a thermodynamic model to predict the phase equilibrium conditions in the hydrate-bearing porous media. The application of this model was implemented by calculating the water activity caused by the sedimentary geometrical constraints (using Eq. (2)) based on their previously constructed Chen-Guo model (Chen and Guo, 1996). In a recent work, Azimi et al. (2021) employed a similar route of modifying water activity based on the vdW-P model. Both of these models were reported to be capable of predicting the formation/dissociation conditions of simple and mixed-gas hydrate in various porous media. The above two models are applicable for the water-filled conditions in the hydrate-bearing media without gas-water interfaces. No research has applied this route in PNM.

## 2.3 Model hypotheses and simulation procedure

Based on the kinetic theory of hydrate formation, a PNM simulator aiming to model the hydrate formation in porous media was developed in this work. In this simulator, the viewpoints of hydrate nucleation and hydrate growth were employed. The water activity of each pore and throat in the pore network is calculated to determine

the hydrate growth order in the pore network. To improve the computation efficiency the following hypotheses were adopted.

(1) The formation of hydrate in porous media can be independently divided into a nucleation process and a subsequent growth process.

(2) The nucleation of hydrate in pores occurs stochastically. Nucleation fraction ($F_n$) is defined as the ratio of the number of nucleated pores to the total pores in the network.

(3) The growth process begins after the nucleation process; the hydrate growth happens following the order of pore-water activity from high to low meanwhile along with the interface between hydrate and water.

(4) Assume that hydrates entirely fill the pores once the hydrate nucleates or forms in the pores or throats. This assumption of either 100% or 0% pore occupancy by hydrates reflects Ostwald ripening effect (Lei et al., 2019), which was also adopted in previous works (Dai and Seol, 2014; Mahabadi et al., 2016; Wang et al., 2015).

(5) Pores or throats occupied by hydrate are assumed to be immobile. The permeability of the model can be calculated by the conductivity relations between network elements (Blunt, 2001, 2017; Zhao et al., 2022).

(6) The influences of the gas-water interface, clay minerals, and other complex controlling factors are neglected in the current vision of the simulator.

Simulations of hydrate formation in our simulator are conducted following the workflow as shown in Fig. 1. Herein, (1) Generate pore networks extracted from CT

images or generate regular networks using a stochastic method (Blunt, 2001), then initialize the water saturation, wettability conditions (contact angle and interfacial tension) of the network elements (pores and throats), and the terminal hydrate saturation. (2) Explore and determine the maximum and minimum water activity in the pore networks ( $A_{w_\max}$ and $A_{w_\min}$ ); the searching index $Sx$ is initialized to be $A_{w_\max}$ . (3) Initiate the nucleation fraction with a value ranging from 0 to 1, and then simulate the hydrate nucleation process using a stochastic algorithm. (4) After the nucleation, explore and determine the network elements that are ready to grow, which count the pores occupied with water neighboring the pores occupied by hydrate. (5) Hydrate growth occurs when $Sx$ is smaller than the water activity of pores in the element-to-grow group. If it occurs, the pore would be translated into pores with hydrate. If not, the pore maintains the condition of water-filling. (6) Update the variables and graphical user interface, then calculate the effective permeability. (7) Check the termination condition whether the hydrate saturation reaches the assigned terminal hydrate saturation. If yes, output the results and terminate the simulation. If no, update the searching index, then make loops for steps (4) to (6) until reaching the terminal hydrate saturation.

Note that the extraction of pore network from CT images was completed using a modified maximal method proposed by Dong and Blunt (2009). The graphical user interface module in our simulator was modified from the open-source PNM code developed by Boujelben (Boujelben et al., 2018). We appreciate the excellent works

shared by these scholars.

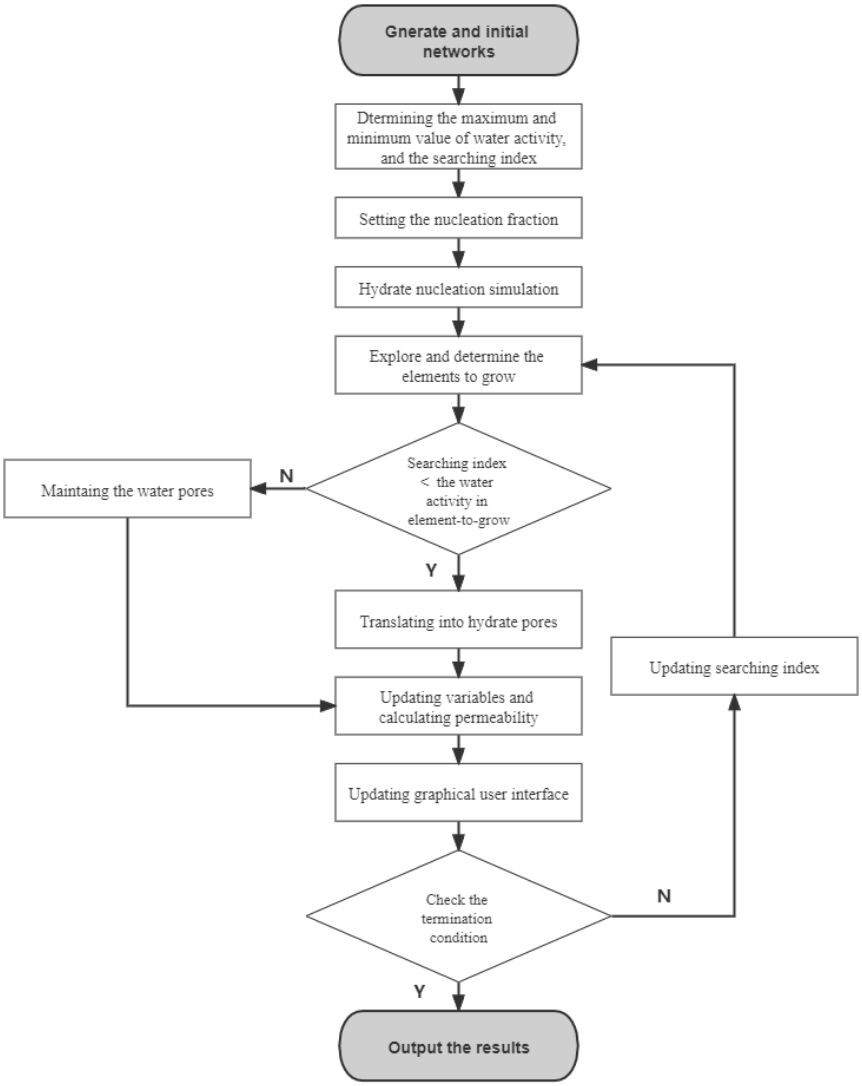


Fig. 1 Workflow for the KT-PNM of hydrate formation and effective permeability calculation

## 3. Simulation Results and Discussion

### 3.1 Influence of model dimension

Given both the 2D model and 3D model are used in the PNM studies of HBS, here we analyze the influence of model dimension on the correlations between effective

permeability and hydrate saturation. Hydrate formation processes are modeled in the regular networks constructed in the forms of 2D and 3D. Basic pore-structure parameters (e.g., pore size distribution range, tortuosity, wettability distribution) are kept the same for these two networks. The nucleation fraction set in the 3D network is 0.02 while the parameter set in the 2D networks ranges from 0.02 to 0.18. The effective permeability results of the 3D network and series of 2D networks have been plotted in Fig. 2. In Fig. 2, the geometrical elements colored with blue represent the pores or throats occupied by water, and the elements colored with white represent the pores or throats occupied by hydrate. Normalized effective permeability is given to compare the results, which defines the ratio of effective permeability to the absolute permeability of the sample. It shows that the normalized effective permeability decreases with the increasing hydrate saturation for 2D and 3D networks. The normalized effective permeability in 2D networks is larger than that of the 3D network when the hydrate saturation is lower than a value of ~ 10 %. When the hydrate saturation is larger than this value, the normalized effective permeability in 2D networks decreases rapidly and shows lower values than that of the 3D network. Moreover, the 2D effective permeability decrease to 0 when the hydrate saturation reaches a range of 20 – 30 % while the 3D effective permeability decreases to 0 until the hydrate saturation reaches the value of ~ 60 %. Based on the results in Fig. 2, the permeability reduction exponents fitted with the Tokyo model are within the range of 7 – 9 for 2D networks and 3.5 for the 3D network.

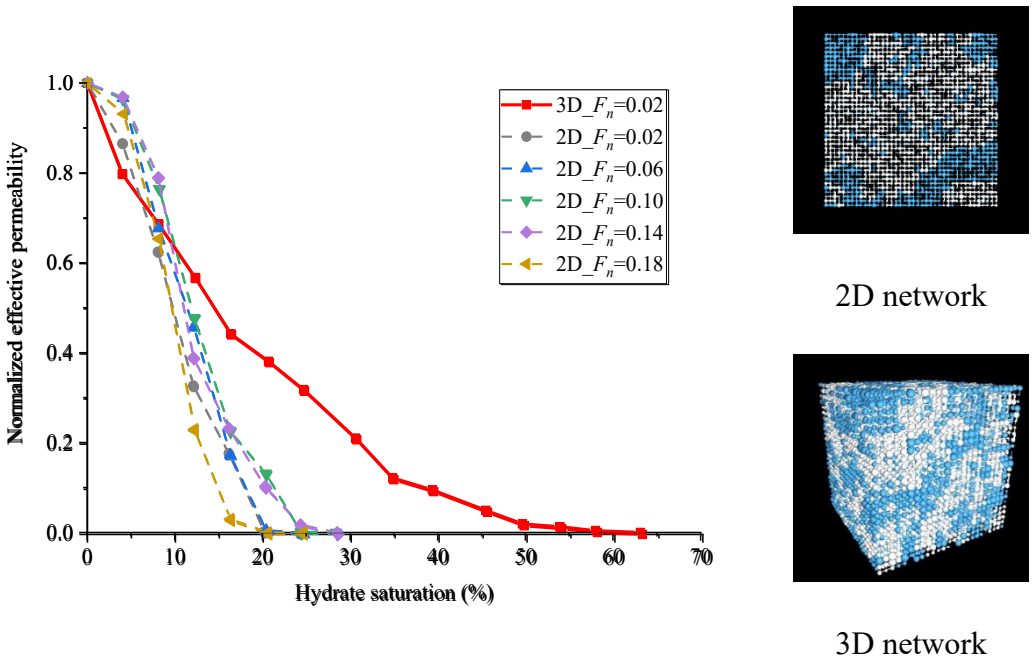


Fig. 2 Comparisons of normalized effective permeability between 2D and 3D networks. The figure on the left shows the normalized effective permeability results; the figures on the right illustrate the comparisons between 2D and 3D regular networks; the geometrical elements colored with blue represent the pores or throats occupied by water, and the elements colored with white represent the pores or throats occupied by hydrate.

## 3.2 Influence of nucleation fraction

To visually explain the influence of nucleation fraction on hydrate formation, hydrate distributions in regular 2D networks formed with different nucleation fraction settings have been plotted in Fig. 3. All the results shown in Fig.3 have the same hydrate saturation of 15 %. The results show that the hydrate distributions formed in the network would be affected by the nucleation fraction. In the cases with low nucleation

fraction (i.e., Figs. 3-a, b, and c), hydrate prefers to accumulate and distribute in partial areas of the network, showing a patchy pattern. In the cases with relatively high nucleation fractions (i.e., Figs. 3-c, d, and e), the formed hydrates preferentially disseminate throughout the network. The effective permeability results calculated from 3D regular networks with different nucleation fractions are plotted in Fig. 4. The normalized effective permeability of all the cases decreases from 1 down to 0 when the hydrate increases from 0 to ~ 60 %; the reducing effect of formed hydrate on effective permeability is more pronounced when the hydrate saturation is smaller than 30% than that of the hydrate saturation being within the range of 30 – 60%. Meanwhile, the effective permeability curves of the cases with a higher nucleation fraction decrease faster under low hydrate saturation than the cases with a lower nucleation fraction. It can be deduced that the effective permeability of the sample with disseminate-distributed hydrate is larger than that of patchy-distributed hydrate for the condition of the same hydrate saturation in the same sample. Based on the calculation results in Fig. 4, the permeability reduction exponent fitted with the Tokyo model increases from 3 to 7 when the nucleation fraction increases from 0.002 to 0.180.

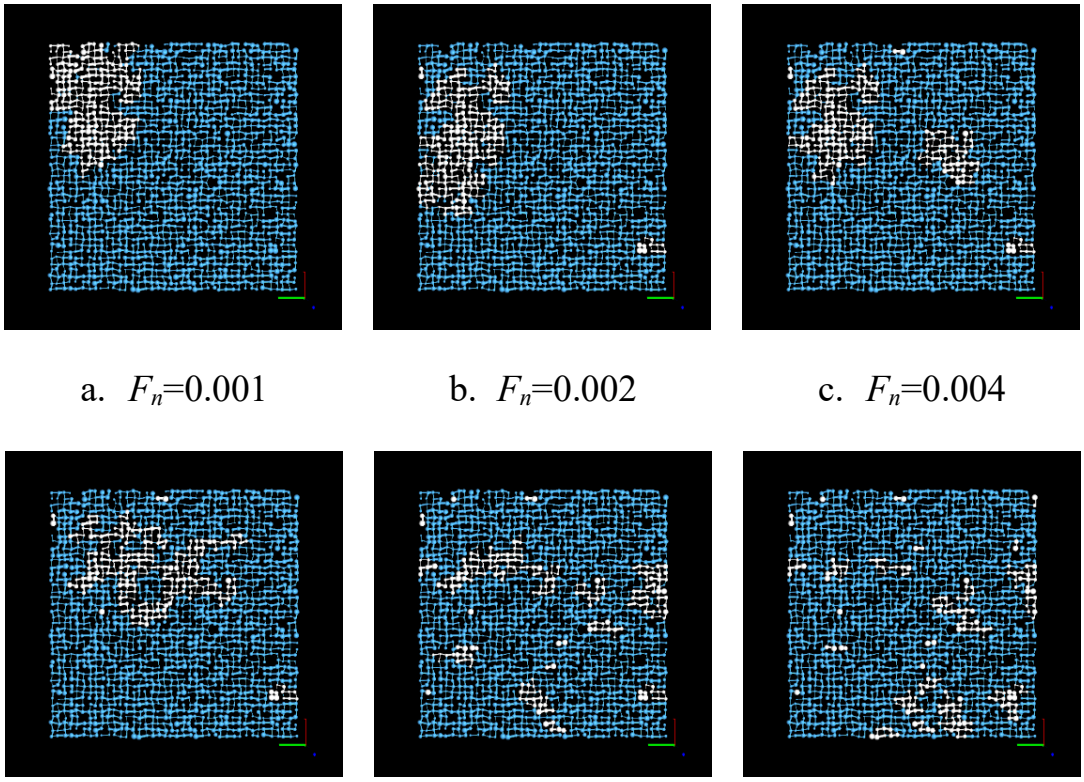

a. $F_n$=0.001 b. $F_n$=0.002 c. $F_n$=0.004

d. $F_n$=0.008 e. $F_n$=0.012 f. $F_n$=0.016

Fig. 3 The distribution of formed hydrates in 2D regular networks in different nucleation fraction settings

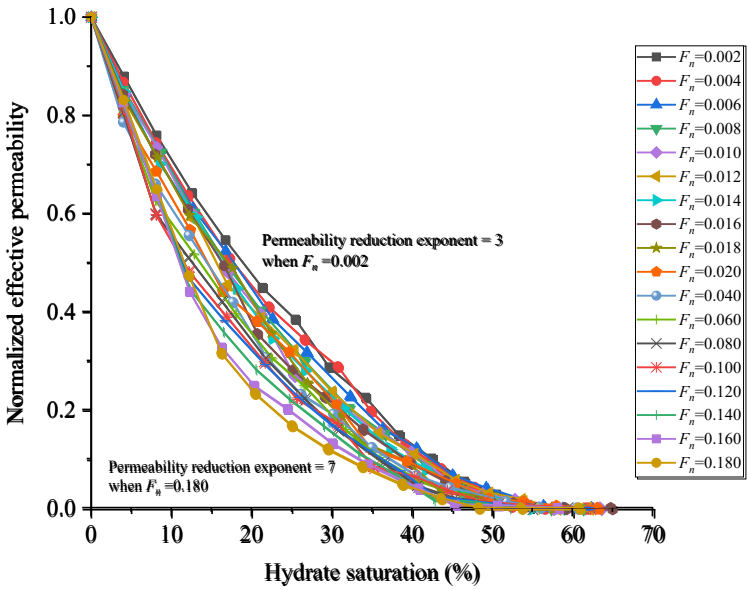


Fig. 4 Calculated normalized effective permeability of 3D regular networks in different

nucleation fraction settings. The permeability reduction exponent fitted with the Tokyo model is 3 when the nucleation fraction is 0.002. And the fitted permeability reduction exponent is 7 when the nucleation fraction is 0.180.

## 3.3 Influence of hydrate growth type during formation

Three types of hydrate growth, including low $A_w$ priority, high $A_w$ priority, and evenly growth, are simulated in this work. The case of low $A_w$ priority means that the hydrate contacting the hydrate-water interface preferentially grows into the neighboring water-pores with lower water activity. The case of high $A_w$ priority means the opposite condition of higher water activity. The case of evenly growth indicates that the hydrate around the hydrate-water interface would evenly grow into the neighboring water-pores with the same priority. Fig. 5 shows the effective permeability results of 3D networks influenced by the hydrate growth type along with the illustrating views of these three growth types in a 2D network. Seen from the 2D illustrating views, hydrates mainly form in the smaller pores under the condition of low $A_w$ priority and form in the larger pores under the condition of high $A_w$ priority; under the condition of evenly growth, the formed hydrates are distributed among the pores in the form of regular clusters. When the hydrate saturation is smaller than ~15 %, the results of calculated effective permeability show slight differences for the three cases. When is the hydrate saturation is in the range of 15 – 60 %, the effective permeability of the case with high $A_w$ priority is larger than that of low $A_w$ priority; the effective permeability of evenly growth type

shows lower values than those of the above two cases.

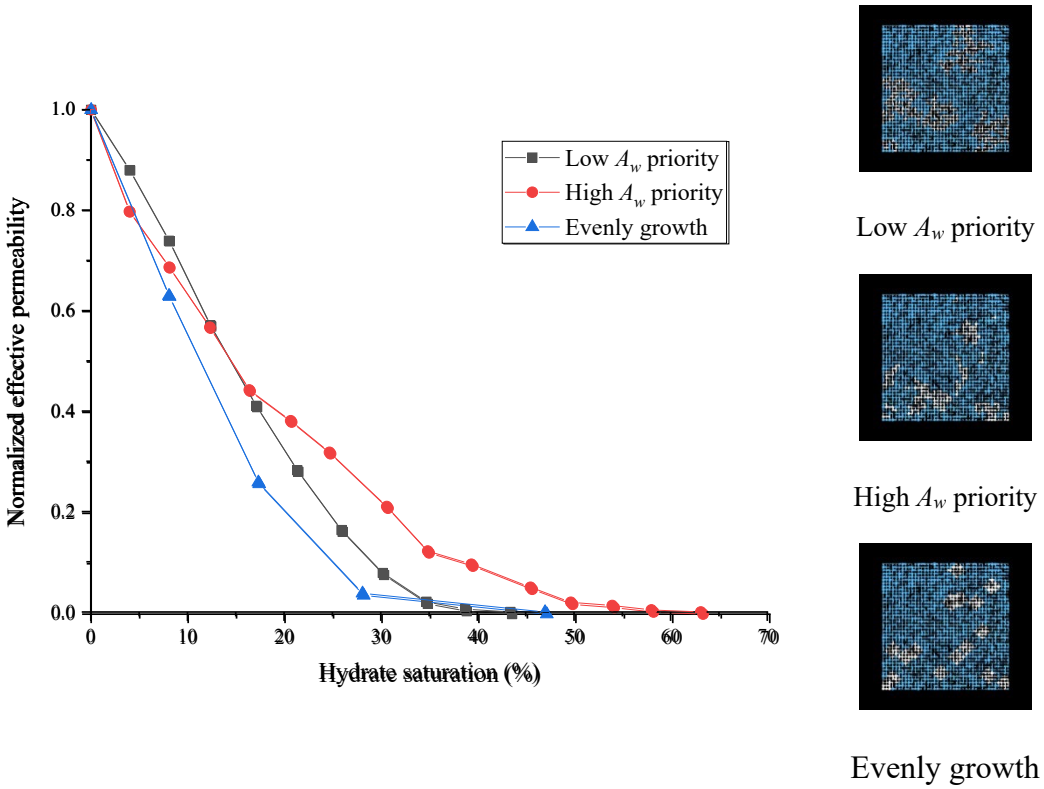


Fig. 5 The effective permeability results of cases with three hydrate growth types in 3D networks (left) and their illustrating views in 2D networks (right). High $A_w$ priority and low $A_w$ priority mean the hydrate preferentially grows into the neighboring water-pores with higher and lower water activity, respectively. And the evenly growth indicates that the hydrate would evenly grow into the neighboring water-pores.

## 3.4 Simulation results in sandy samples

All the simulation cases listed in Sections 3.1 – 3.3 are completed in regular networks, further simulations based on the networks extracted from CT images of sandy samples are documented in the following.

### 3.4.1 CT scanning and image processing

Seven sandy samples were selected to obtain CT gray-scale images and generate pore networks for the hydrate formation simulation. These sandy samples were synthesized by compacting quartz sands with different grain sizes into an aluminum vessel. CT scans of these samples were conducted using a Phoenix, v|tome|x version CT scanner in Qingdao Institution of Marine Geology. The size of the representative effective volume (REV) cropped for image processing and further simulation is 400×400×400 pixel$^3$. Other parameters including the image resolution have been listed in Table 1. 2D CT gray-scale slices of used samples are given in Fig. 6.

The obtained 2D grayscale images were reconstructed to 16-bit three-dimensional (3D) grayscale images using a software package "Datos|rec" developed by Phoenix Contact company. Subsequent image noise reduction, image filtering, and phase segmentation were completed using the software Avizo 9.7 developed by Thermo Fisher Scientific. The image filtering method employed in the processing was the non-local means algorithm (Liu et al., 2008). And the phase segmentation between the sand phase and fluid phase was completed using the interactive thresholding method based on the grayscale differences between phases. To further analyze the distribution characteristics of sand grains, the segmented sand phase is separated into sand grains based on the topological relations of gray areas (Fig. 7). The grain size distributions of the samples calculated from image data are plotted in Fig. 8. It shows that the grain radii of used samples are distinctively distributed in the range of 0 – 800 μm; the grain

radius of samples generally increases from Sample #1 to Sample #7. The grain-size distribution of the used samples is consistent with the natural sandy HBSs (Ito et al., 2015; Kraemer et al., 2000; Minagawa et al., 2012; Winters et al., 2011; Yamamoto et al., 2014).

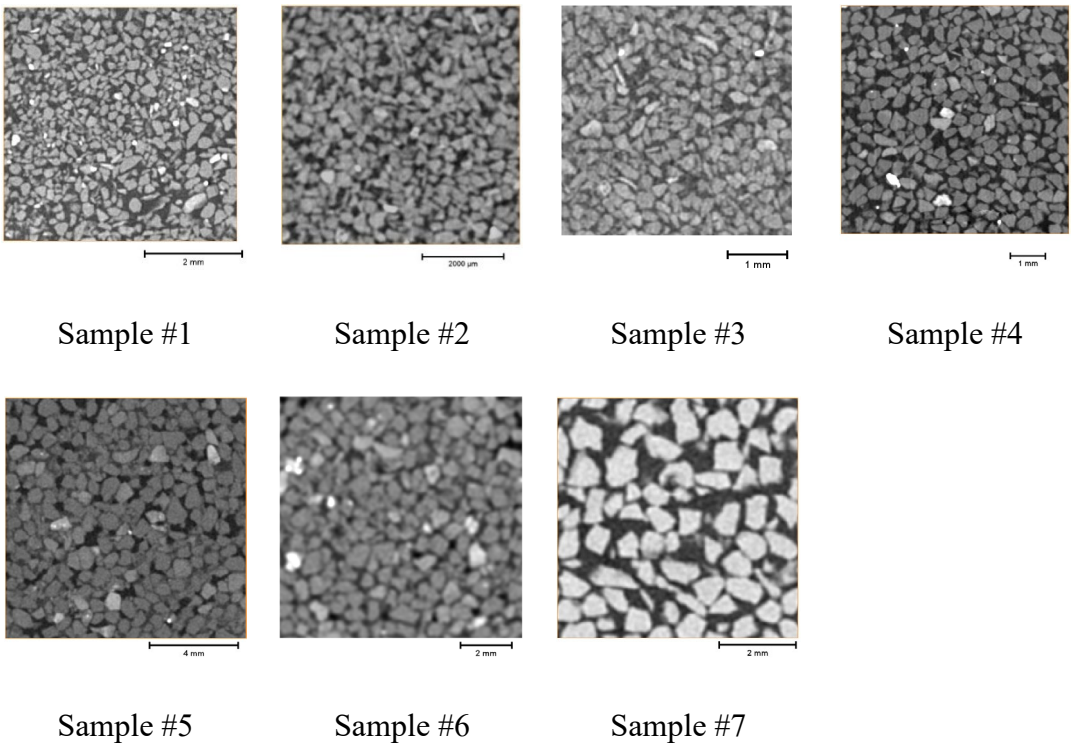


Fig. 6 Slices of gray-scale CT images for the seven sandy samples. The gray area with a clear boundary in the images is sands; the dark area may include the gas phase and water phase; the size of these present CT slices is 400×400×1 pixel$^3$; the resolution of each slice and other parameters can be found in Table 1.

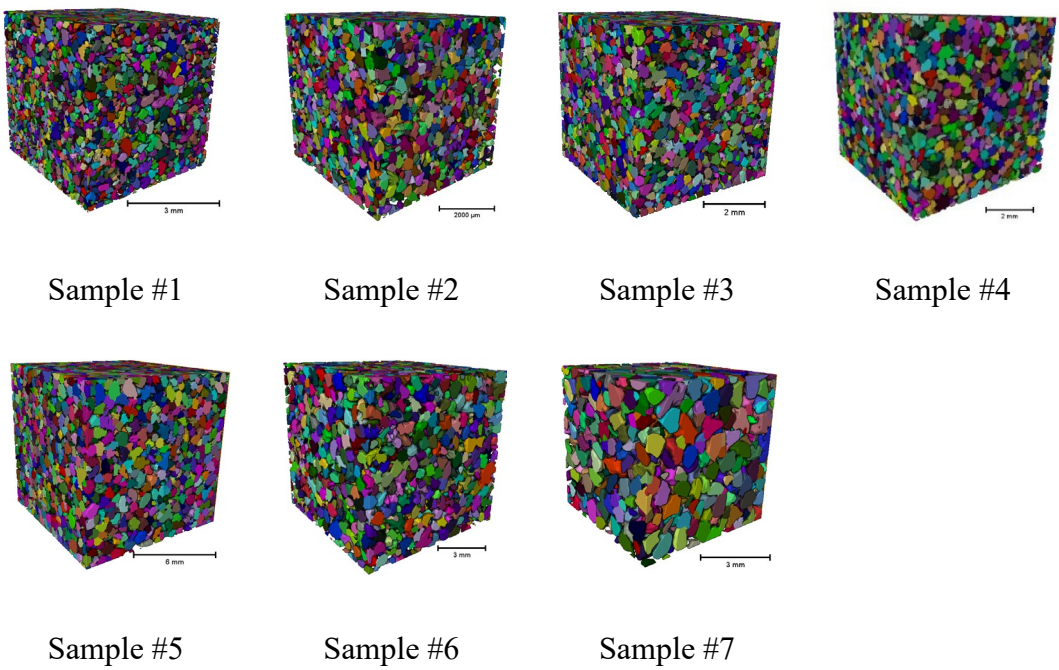


Fig. 7 3D presentation of separated sand grains extracted from CT images for seven sandy samples. Adjacent grains in each sample are colored with different colors.

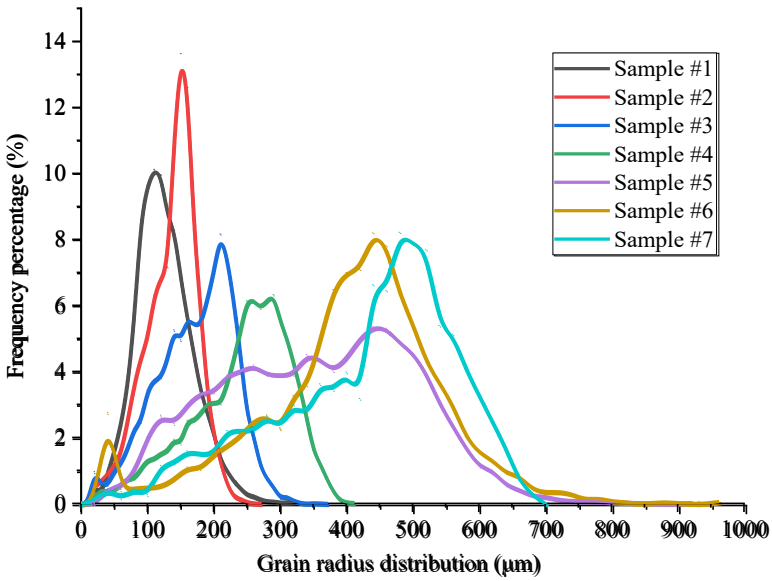


Fig. 8 Grain radius distribution of the simulated samples. Frequency percentage on the Y coordinate axis means the quantity percentage of grains with a certain radius against the number of total grains.

Table 1 Properties of the simulated samples calculated from CT images

| **Sample NO.** | **Porosity (%)** | **Geometric tortuosity** | **Image resolution (μm)** | **Max grain radius (μm)** | **Mean grain radius (μm)** | **Max pore radius (μm)** | **Mean pore radius (μm)** |
|---|---|---|---|---|---|---|---|
| Sample# 1 | 45.6 | 1.26 | 12.0 | 280 | 121 | 210 | 73 |
| Sample# 2 | 39.1 | 1.32 | 13.5 | 230 | 130 | 210 | 80 |
| Sample# 3 | 34.9 | 1.44 | 12.5 | 300 | 167 | 290 | 101 |
| Sample# 4 | 34.5 | 1.47 | 16.0 | 390 | 236 | 310 | 105 |
| Sample# 5 | 34.3 | 1.46 | 37.3 | 680 | 347 | 460 | 158 |
| Sample# 6 | 38.8 | 1.49 | 23.7 | 720 | 397 | 540 | 220 |
| Sample# 7 | 42.2 | 1.44 | 15.8 | 660 | 420 | 550 | 240 |

### 3.4.2 Hydrate saturation vs. normalized effective permeability

The hydrate formation processes in the seven sandy samples are simulated using the developed KT-PNM. These simulations are implemented in the 3D dimension following the hydrate growth type of high $A_w$ priority. For the reason that the nucleation fraction cannot be predicted or measured, this parameter is assumed to be a constant value of 0.02 for seven cases by comparing the simulation results of hydrate distribution with CT images from the literature (Lei et al., 2018, 2019). Fig. 9 shows the graphical results of simulations under the same condition of hydrate saturation being 60 % for 7 samples. And Fig. 10 illustrates the effective permeability results as a function of hydrate saturation. It can be observed that both the hydrate distribution in the networks

and the effective permeability curves show noticeable differences for various samples. We have made correlation analyses between the normalized effective permeability results and the pore-structure parameters, including maximum or minimum pore radius, mean pore radius, pore tortuosity, and porosity. No clear correlations can be determined. However, we found that the permeability reduction exponents fitted with the Tokyo model in all the simulated samples are in a limited range of 3 – 4. Possible reasons causing the similar permeability reduction exponents for seven samples are analyzed as follows. Firstly, all the effective permeability results in Fig. 10 have been normalized, which means the position of the curves plotted is little affected by the mean pore size of the samples. The changes in curves show the influences of pore structures and hydrate distribution on the normalized effective permeability. And the growth of hydrate in the pore spaces can be influenced by the hydrate nucleation properties, connectivity of pores, and the pore size distribution, as documented in Section 2. In Figs. 6 – 7, most of the pores in all the sandy samples are well connected and the PSD curves of the seven samples are all close to the normal distribution curve. In this case, the changes of normalized effective permeability as a function of hydrate saturation would be similar in trend. The permeability reduction exponent range of 3 – 4 in the Tokyo model permits a good match between the normalized effective permeability and hydrate saturation for sandy samples would be reasonable.

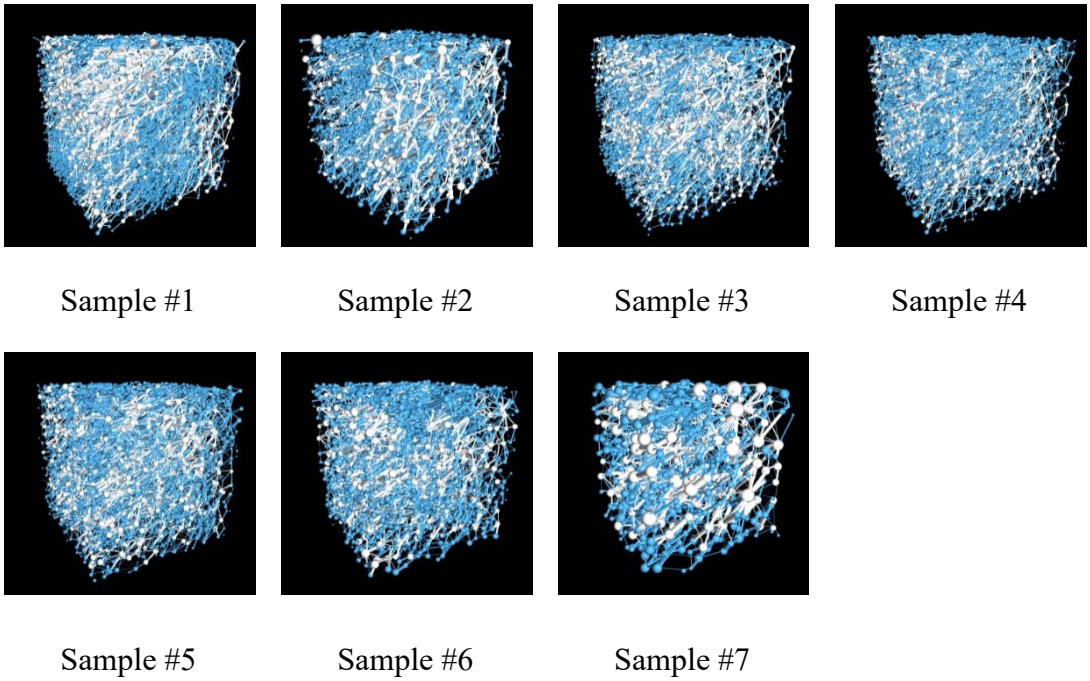


Fig. 9 Hydrate distributions obtained from KT-PNM for the seven sandy samples. White areas represent the network elements occupied with hydrate. And blue areas mean the network elements occupied by the water phase.

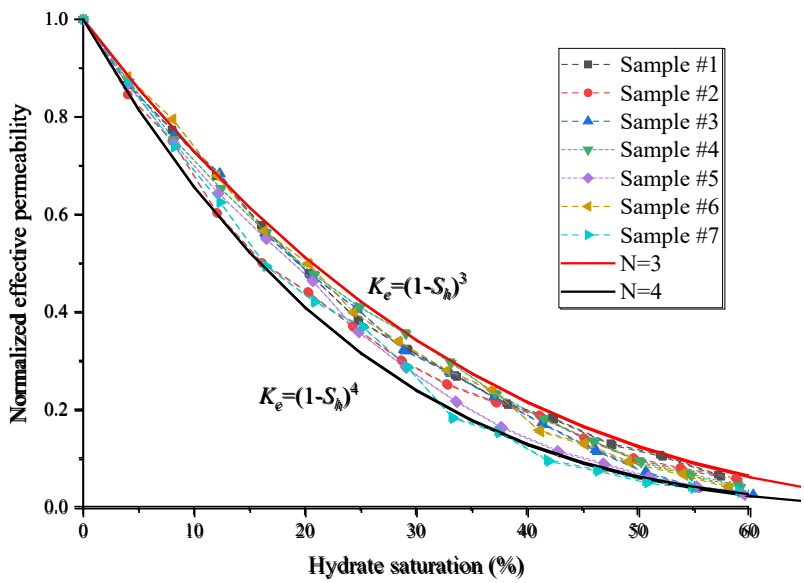


Fig. 10 The relationships between normalized effective permeability and hydrate saturation calculated from KT-PNM for seven sandy samples

To validate the obtained parameter values of permeability reduction exponent, we compared the simulation results with the experimental results of sandy samples in the literature (Fig. 11-a). The red and black lines in the figure represent the normalized effective permeability curves with the permeability reduction exponent equals 3 and 4, correspondingly. It reveals that the experimental normalized effective permeability data are basically located in the areas closed by the exponent lines. Considering the differences in the experimental methods and sample property, the results concluded from numerical simulations can be considered to agree well with the experiments. However, note that the drawn conclusion of permeability reduction exponent can hardly apply to the predictions of effective permeability in silty HBS or sandy HBS containing clay minerals. The permeability in these media behaves differently from the hydrate saturation compared to the sandy sediments (Fig. 11-b). Sample property and testing methods supporting the experimental data plotted in Fig. 11 are listed in Table 2.

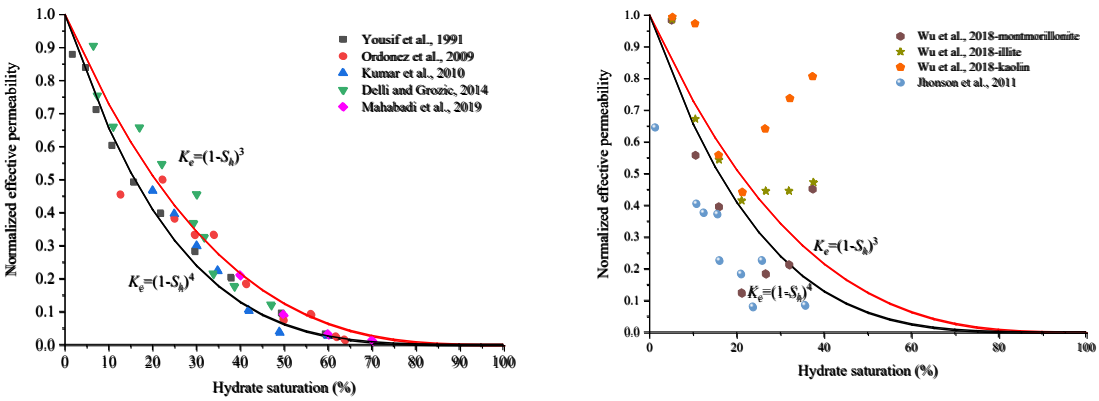


(a) Simulation results vs. experimental (b) Simulation results vs. experimental

results of sandy samples results of silty samples

Fig. 11 Comparison of normalized effective permeability as a function of hydrate saturation between KT-PNM simulations and the experimental results from the literature

Table 2 Summary of permeability tests in the hydrate-bearing sediments obtained from literature

| **Literature** | **Sample property** | **Hydrate synthesizing method** | **Permeability measuring method** |
|---|---|---|---|
| Yousif et al. (1991) | Berea sandstone with a porosity of 18.8 % | Methane hydrate, excess-gas method | Gas-flow method |
| Ordonez et al. (2009) | Ottawa sand | R-11 ($CCl_3F$) hydrate | Water-flow method |
| Kumar et al. (2010) | Glass beads with a diameter range of 88.9 – 149.8 μm | $CO_2$ hydrate, excess-gas method | Gas-flow method |
| Delli and Grozic (2014) | Ottawa 20/30 silica sand with a grain size distribution of 600 – 800 μm | $CO_2$ hydrate, excess-gas method | Water-flow method |
| Mahabadi et al. (2019) | Three different groups of sands | THF hydrate | Water-flow method |
| Jhonson et al. | Unconsolidated samples from the | Methane hydrate, | Brine-flow |

| | | | |
|---|---|---|---|
| (2011) | Mount Elbert site on the Alaska North Slope (ANS) | excess-gas method | method |
| Wu et al. (2018) | Montmorillonite with median diameter 8.27 μm; kaolin with median diameter 6.91 μm; illite with median diameter 3.53 μm | Methane hydrate, ice-seed method | Gas-flow method |

### 3.4.3 Hydrate saturation vs. effective permeability

To predict the evolution of effective permeability as a function of hydrate saturation, Eq. (3) was deduced by coupling the Kozeny-Carman equation with the Tokyo model.

$$K_e = m\frac{\phi^3 r_g^{\ 2}}{\tau}(1-S_h)^n, \tag{3}$$

where $\phi$ is the porosity of the sample, $r_g$ is the mean grain radius, $\tau$ is the mean tortuosity of pore spaces, $m$ and $n$ indicates the pore-structure parameter affecting the fluid flow and permeability reduction exponent as introduced in the Tokyo model. For sandy media, $m$ was determined to be 0.6 after fitting with the simulation results and $n$ was determined to be 3.5 taking a mean value of the range 3 – 4. The equation for predicting the effective permeability as a function of hydrate saturation in sandy media can be expressed as Eq. (4).

$$K_e = 0.6\frac{\phi^3 r^2}{\tau}(1-S_h)^{3.5} \tag{4}$$

A comparison between effective permeability results calculated from Eq. (4) and experimental results from previous literature is plotted in Fig. 12. It should be noted

that effective permeability results of hydrate-bearing sandy samples were rarely reported in previous works. As a result, only two sets of experimental results (Kumar et al., 2010; Pan et al., 2010) are plotted in Fig. 12. From the comparison, the model calculation results show good agreement with the experiments. However, this agreement merely proved the reliability of Eq. (4) in predicting the effective permeability of sandy HBS to a certain degree. Further validation with more experimental results is still necessary for future studies. There is still one more issue that should be explained. Most of the reported experimental results, including all these in Fig. 11 and Fig. 12, were actually conducted in different experimental conditions. These differences, as listed in Table 2, may include the property of sandy samples, type of guest-molecular materials, hydrate synthesizing method, and permeability measuring method. Any of these differences would affect the accuracy of the obtained results. In this case, physical experiment of permeability measurement with higher accuracy would be helpful for improving the prediction of PNM in HBS.

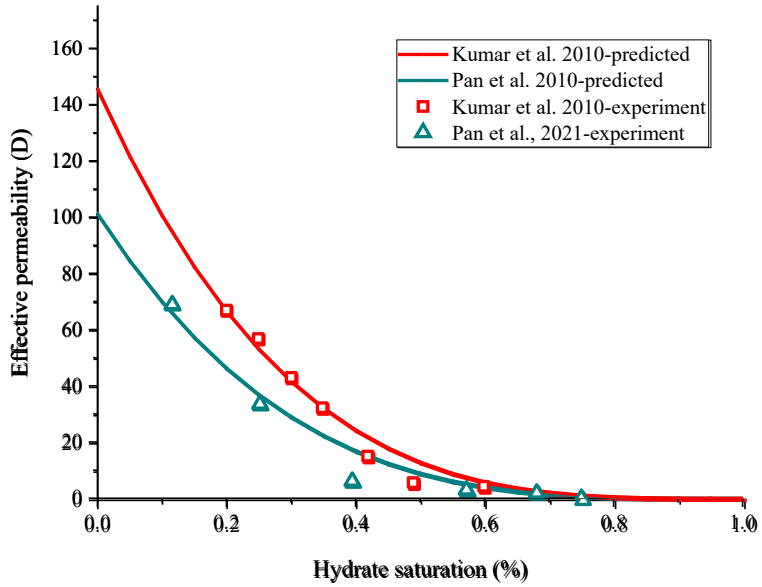


Fig. 12 Comparison of effective permeability as a function of hydrate saturation between equation calculation and experimental results from literature

## 4. Conclusions

In this work, we developed a KT-PNM to simulate the hydrate formation and analyze the changes in effective permeability as a function of hydrate saturation in sandy HBS. In the developed KT-PNM, the hydrate nucleation and hydrate growth conceptions in the hydrate formation kinetic theory are physically embedded. Simulation results of regular networks show that the 2D PNM leads to an underestimated permeability or overestimated permeability reduction exponent compared to the 3D PNM, thus failing to provide accurate predictions of permeability in HBS. The amount of nucleation pores determines the distribution of formed hydrates in the pore network and further impacts the evolution of effective permeability with hydrate saturation. Under the same condition of hydrate saturation, the reduction effect

of disseminate-distributed hydrates formed with higher nucleation fraction is stronger than that of patchy-distributed hydrates formed with lower nucleation fraction. Simulation results of extracted networks from seven sandy samples show that the changes in the normalized effective permeability as a function of hydrate saturation are similar for different sandy samples. The permeability reduction exponent for sandy HBS fitted with the Tokyo model is determined to be within a range of 3 – 4 based on the simulations. This result further permits the modification of the Kozeny-Carman equation and the Tokyo model to predict the effective permeability in sandy HBS: $K_e = 0.6\frac{\phi^3 r_g^{\ 2}}{\tau}(1-S_h)^{3.5}$ . This equation shows the combined effects of the pore-structure features of sediment and hydrate formation on effective permeability, of which the prediction results agree well with the reported experiments.

The developed KT-PNM proposed in this work is not merely appliable for sandy HBS. The route of model development can be extended to other types of HBSs if adequate experimental data are available for verification. Moreover, the model and simulation results in this work are relevant to the research of kinetics, thermodynamics, property analysis, and hydrate production numerical simulation related to hydrate formed in the hydrate-bearing sediment.

## Declaration of competing interest

The authors declare that they have no known competing financial interests or personal relationships that could have appeared to influence the work reported in this paper.

## Acknowledgments

This work is supported by the National Natural Science Foundation of China (grant numbers (42006181, 42176212, 41876051), the Natural Science Foundation of Shandong Province (ZR2020QE109), and the Marine S&T Fund of Shandong Province for Pilot National Laboratory for Marine Science and Technology (Qingdao) (2021QNLM020002).

## Data availability statements

All the CT data supporting the simulations in this work can be downloaded from the Mendeley repository (https://data.mendeley.com/datasets/v3b9wxp2tf/1).

## References


Ai, L., Zhao, J., Wang, J., Song, Y., 2017. Analyzing permeability of the irregular porous media containing methane hydrate using pore network model combined with CT. Energy Procedia 105, 4802–4807.

Andrew, J., Shirish, P., Abhijit, D., 2011. Experimental investigation of gas-water relative permeability for gas-hydrate-bearing sediments from the Mount Elbert gas hydarte stratigrapgic test well, Alaska North Slope. Mar. Pet. Geol. 28(2), 419–426.

Azimi, A., Javanmardi, J., Mohammadi, A.H., 2021. Development of thermodynamic frameworks for modeling of clathrate hydrates stability conditions in porous media. J. Mol. Liq. 329, 115463.

Blunt, M.J., 2001. Flow in porous media—pore-network models and multiphase flow. Curr. Opin. Colloid Interface Sci. 6(3), 197–207.

Blunt, M.J. 2017. Multiphase flow in permeable media: A pore-scale perspective. Cambridge University Press.

Boswell, R., Collett, T.S., 2011. Current perspectives on gas hydrate resources. Energy Environ. Sci. 4(4), 1206–1215.

Boswell, R., Hancock, S., Yamamoto, K., Collett, T., Pratap, M., Lee, S.-R., 2020. Natural gas hydrates: status of potential as an energy resource. Future Energy 111–131.

Boujelben, A. H., McDougall, S., Watson, M., Bondino, I., Agenet, N., 2018. Pore

network modelling of low salinity water injection under unsteady-state flow conditions. J. Pet. Sci. Eng. 165, 462–476.

Cai, J., Xia, Y., Lu, C., Bian, H., Zou, S., 2020. Creeping microstructure and fractal permeability model of natural gas hydrate reservoir. Mar. Pet. Geol. 115, 104282.

Chen, G., Guo, T., 1996. Thermodynamic modeling of hydrate formation based on new concepts. Fluid Phase Equilib. 122(1-2), 43–65.

Chen, L., Sun, C., Chen, G., Nie, Y., 2010. Thermodynamics model of predicting gas hydrate in porous media based on reaction− adsorption two-step formation mechanism. Ind. Eng. Chem. Res. 49(8), 3936–3943.

Chen, X., Espinoza, D.N., 2018. Surface area controls gas hydrate dissociation kinetics in porous media. Fuel 234, 358–363.

Chen, X., Verma, R., Espinoza, D.N., Prodanović, M., 2018. Pore-Scale determination of gas relative permeability in hydrate-bearing sediments using X-ray computed micro-tomography and Lattice Boltzmann method. Water Resour. Res. 54(1), 600–608.

Clarke, M.A., Pooladi-Darvish, M., Bishnoi, P.R., 1999. A method to predict equilibrium conditions of gas hydrate formation in porous media. Ind. Eng. Chem. Res. 38(6), 2485–2490.

Cui, Y., Lu, C., Wu, M., Peng, Y., Yao, Y., Luo, W., 2018. Review of exploration and production technology of natural gas hydrate. Adv. Geo-Energy Res. 2(1), 53–62.

Dai, S., Santamarina, J.C., Waite, W.F., Kneafsey, T.J., 2012. Hydrate morphology: Physical properties of sands with patchy hydrate saturation: patchy hydrate saturation. J. Geophys. Res. 117(11), B11205.

Dai, S., Seol, Y., 2014. Water permeability in hydrate-bearing sediments: A pore-scale study. Geophys. Res. Lett. 41(12), 4176–4184.

Delli, M.L., Grozic, J.L., 2014. Experimental determination of permeability of porous media in the presence of gas hydrates. J. Pet. Sci. Eng. 120, 1–9.

Delli, M.L., Grozic, J.L., 2013. Prediction performance of permeability models in gas-hydrate-bearing sands. SPE J. 18(2), 274–284.

Dong, H., Blunt, M.J., 2009. Pore-network extraction from micro-computerized-tomography images. Phys. Rev. E 80(3), 036307.

Englezos, P., Kakogerakis, N., Dholabhai, P.N., Bishnoi, P.R., 1987. Kenetics of formation of methane and ethane gas hydrates. Chem. Eng. Sci. 42(11), 2647–2658.

Golsanami, N., Jayasuriya, M.N., Yan, W., Fernando, S.G., Liu, X., Cui, L., Zhang, X., Yasin, Q., Dong, H., Dong, X., 2022. Characterizing clay textures and their impact on the reservoir using deep learning and Lattice-Boltzmann simulation applied to SEM images. Energy 240, 122599.

Gupta, S., Helmig, R., Wohlmuth, B., 2015. Non-isothermal, multi-phase, multi-component flows through deformable methane hydrate reservoirs. Comput. Geosci. 19(5), 1063–1088.

Ito, T., Komatsu, Y., Fujii, T., Suzuki, K., Egawa, K., Nakatsuka, Y., Konno, Y., Yoneda, J., Jin, Y., Kida, M., 2015. Lithological features of hydrate-bearing sediments and their relationship with gas hydrate saturation in the eastern Nankai Trough, Japan. Mar. Pet. Geol. 66, 368–378.

Kraemer, L.M., Owen, R.M., Dickens, G.R. 2000. Lithology of the upper gas hydrate zone, Blake Outer Ridge: A link between diatoms, porosity, and gas hydrate. Proceedings of the Ocean Drilling Program. Scientific Results, Texas A&M University, 164, 229–236.

Kleinberg, R.L., 1999. 9. Nuclear Magnetic Resonance, in: Experimental Methods in the Physical Sciences. Elsevier, 337–385.

Konno, Y., Jin, Y., Uchiumi, T., Nagao, J., 2013. Multiple-pressure-tapped core holder combined with X-ray computed tomography scanning for gas–water permeability measurements of methane-hydrate-bearing sediments. Rev. Sci. Instrum. 84(6), 064501.

Konno, Y., Oyama, H., Nagao, J., Masuda, Y., Kurihara, M., 2010. Numerical analysis of the dissociation experiment of naturally occurring gas hydrate in sediment cores obtained at the Eastern Nankai Trough, Japan. Energy Fuels 24(12), 6353–6358.

Kou, X., Li, X.-S., Wang, Y., Wan, K., Chen, Z.-Y., 2021. Microscale experiment and pore-network modeling analysis of growth habit, pore structure, and permeability of hydrate-bearing sediments. Energy Fuels 35(10), 8773–8785.

Kumar, A., Maini, B., P.R. Bishnoi, Clarke, M., Zatsepina, O., Srinivasan, S., 2010. Experimental determination of permeability in the presence of hydrates and its effect on the dissociation characteristics of gas hydrates in porous media. J. Pet. Sci. Eng. 70, 114–122.

Kvamme, B., 2021. Kinetics of hydrate formation, dissociation and reformation. Chemical Thermodynamics and Thermal Analysis 1–2, 100004.

Lei, L., Santamarina, J.C., 2018. Laboratory strategies for hydrate formation in fine-grained sediments. J. Geophys. Res. Solid Earth 123(4), 2583–2596.

Lei, L., Seol, Y., Choi, J.-H., Kneafsey, T.J., 2019. Pore habit of methane hydrate and its evolution in sediment matrix – Laboratory visualization with phase-contrast micro-CT. Mar. Pet. Geol. 104, 451–467.

Lei, L., Seol, Y., Jarvis, K., 2018. Pore-scale visualization of methane hydrate-bearing sediments with micro-CT. Geophys. Res. Lett. 45(11), 5417–5426.

Li, J., Ye, J., Qin, X., Qiu, H., Wu, N., Lu, H., Xie, W., Lu, J., Peng, F., Xu, Z., 2018. The first offshore natural gas hydrate production test in South China Sea. China Geology 1(1), 5–16.

Li, Y., Liu, L., Jin, Y., Wu, N., 2021. Characterization and development of marine natural gas hydrate reservoirs in clayey-silt sediments: A review and discussion. Adv. Geo-Energy Res. 5(1), 75–86.

Liu, L., Dai, S., Ning, F., Cai, J., Liu, C., Wu, N., 2019. Fractal characteristics of unsaturated sands− implications to relative permeability in hydrate-bearing

sediments. J. Nat. Gas Sci. Eng. 66, 11–17.

Liu, L., Zhang, Z., Li, C., Ning, F., Liu, C., Wu, N., Cai, J., 2020. Hydrate growth in quartzitic sands and implication of pore fractal characteristics to hydraulic, mechanical, and electrical properties of hydrate-bearing sediments. J. Nat. Gas Sci. Eng. 75, 103109.

Liu, X., Flemings, P.B., 2007. Dynamic multiphase flow model of hydrate formation in marine sediments. J. Geophys. Res. Solid Earth 112(B3), B03101.

Liu, Y.-L., Wang, J., Chen, X., Guo, Y.-W., Peng, Q.-S., 2008. A robust and fast non-local means algorithm for image denoising. J. Comput. Sci. Tech-CH 23(2), 270–279.

Ma, J., Sanchez, J.P., Wu, K., Couples, G.D., Jiang, Z., 2014. A pore network model for simulating non-ideal gas flow in micro-and nano-porous materials. Fuel 116, 498–508.

Mahabadi, N., Dai, S., Seol, Y., Jang, J., 2019. Impact of hydrate saturation on water permeability in hydrate-bearing sediments. J. Pet. Sci. Eng. 174, 696–703.

Mahabadi, N., Dai, S., Seol, Y., Sup Yun, T., Jang, J., 2016. The water retention curve and relative permeability for gas production from hydrate-bearing sediments: pore-network model simulation: Water retention and permeability. Geochem. Geophys. Geosyst. 17(8), 3099–3110.

Masuda, Y., 1999. Modeling and experimental studies on dissociation of methane gas hydrates in Berea sandstone cores, in: Proceedings of the Third International

Gas Hydrate Conference.

Minagawa, H., Egawa, K., Sakamoto, Y., Komai, T., Tenma, N., Narita, H., 2012. Characterization of hydraulic permeability and pore-size distribution of methane hydrate-bearing sediment using proton nuclear magnetic resonance measurement. International Journal of Offshore and Polar Engineering.

Minagawa, H., Nishikawa, Y., Ikeda, I., Miyazaki, K., Takahara, N., Sakamoto, Y., Komai, T., Narita, H., 2008. Characterization of sand sediment by pore size distribution and permeability using proton nuclear magnetic resonance measurement. J. Geophys. Res. 113(B7), B07210.

Moridis, G.J., Collett, T.S., Pooladi-Darvish, M., Hancock, S., Santamarina, C., Boswell, R., Kneafsey, T., Rutqvist, J., Kowalsky, M.B., Reagan, M.T., 2011. Challenges, uncertainties, and issues facing gas production from gas-hydrate deposits. SPE Reserv. Evaluation Eng. 14(1), 76–112.

Moridis, G.J., Reagan, M.T., Queiruga, A.F., 2019. Gas Hydrate Production Testing: Design Process and Modeling Results, in: Offshore Technology Conference. Presented at the Offshore Technology Conference, Offshore Technology Conference, Houston, Texas, United States.

Myerson, A., 2002. Handbook of industrial crystallization. Butterworth-Heinemann, Oxfordshire.

Ordonez, C., Grozic, J., Chen, W., 2009. Permeability of Ottawa sand specimens containing R-11 gas hydrates. Presented at the The 62. Canadian geotechnical

conference and 10. joint CGS/IAH-CNC groundwater conference, Halifax, Canada, 604–608.

Pan, L., Lei, L., Seol, Y. 2021. Pore-scale influence of methane hydrate on permeability of porous media. J. Nat. Gas Sci. Eng. 87, 103758.

Reagan, M.T., Moridis, G.J., 2007. Oceanic gas hydrate instability and dissociation under climate change scenarios. Geophys. Res. Lett. 34(22), L22709(1-5).

Ren, X., Guo, Z., Ning, F., Ma, S., 2020. Permeability of hydrate-bearing sediments. Earth Sci. Rev. 202, 103100.

Ruppel, C.D., Kessler, J.D., 2017. The interaction of climate change and methane hydrates: Climate-hydrates interactions. Rev. Geophys. 55(1), 126–168.

Silin, D., Patzek, T., 2006. Pore space morphology analysis using maximal inscribed spheres. Physica A 371(2), 336–360.

Sloan Jr, E.D., Koh, C.A., 2007. Clathrate hydrates of natural gases. CRC press, Boca Raton.

Sun, J., Dong, H., Arif, M., Yu, L., Zhang, Y., Golsanami, N., Yan, W., 2021. Influence of pore structural properties on gas hydrate saturation and permeability: A coupled pore-scale modelling and X-ray computed tomography method. J. Nat. Gas Sci. Eng. 88, 103805.

Tamaki, M., Fujii, T., Suzuki, K., 2017. Characterization and prediction of the gas hydrate reservoir at the second offshore gas production test site in the eastern Nankai Trough, Japan. Energies 10(10), 1678.

Van der Waals, J.A., Platteeuw, J.C., 1959. Clathrate solutions. Adv. Chem. Phys. 2, 2–59.

Waite, W.F., Kneafsey, T.J., Winters, W.J., Mason, D.H., 2008. Physical property changes in hydrate-bearing sediment due to depressurization and subsequent repressurization. J. Geophys. Res. Solid Earth 113(B7).

Waite, W.F., Santamarina, J.C., Cortes, D.D., Dugan, B., Espinoza, D.N., Germaine, J., Jang, J., Jung, J.W., Kneafsey, T.J., Shin, H., 2009. Physical properties of hydrate-bearing sediments. Rev. Geophys. 47(4), 465–484.

Wan, Y., Wu, N., Chen, Q., Li, W., Hu, G., Huang, L., Ouyang, W., 2022. Coupled thermal-hydrodynamic-mechanical–chemical numerical simulation for gas production from hydrate-bearing sediments based on hybrid finite volume and finite element method. Comput. Geotech. 145, 104692.

Wang, D., Wang, C., Li, C., Liu, C., Lu, H., Wu, N., Hu, G., Liu, L., Meng, Q., 2018. Effect of gas hydrate formation and decomposition on flow properties of fine-grained quartz sand sediments using X-ray CT based pore network model simulation. Fuel 226, 516–526.

Wang, J., Zhao, J., Zhang, Y., Wang, D., Li, Y., Song, Y., 2015. Analysis of the influence of wettability on permeability in hydrate-bearing porous media using pore network models combined with computed tomography. J. Nat. Gas Sci. Eng. 26, 1372–1379.

Wang, Y., Yang, Y., Wang, K., Tao, L., Liu, J., Wang, C., Yao, J., Zhang, K., Song, W.,

2020. Changes in relative permeability curves for natural gas hydrate decomposition due to particle migration. J. Nat. Gas Sci. Eng. 84, 103634.

Winters, W., Walker, M., Hunter, R., Collett, T., Boswell, R., Rose, K., Waite, W., Torres, M., Pati, S., Dandekar, A. 2011. Physical properties of sediment from the Mount Elbert gas hydrate stratigraphic test well, Alaska North Slope. Mar. Pet. Geol. 28, 361–380.

Wu, N., Li, Y., Wan, Y., Sun, J., Huang, L., Mao, P., 2021. Prospect of marine natural gas hydrate stimulation theory and technology system. Nat. Gas Ind. B 8(2), 173–187.

Wu, Z., Li, Y., Sun, X., Wu, P., Zheng, J., 2018. Experimental study on the effect of methane hydrate decomposition on gas phase permeability of clayey sediments. Appl. Energy 230, 1304–1310.

Xu, Y., Seol, Y., Jang, J., Dai, S., 2017. Water and gas flows in hydrate-bearing sediments, in: Geotechnical Frontiers 2017. Presented at the Geotechnical Frontiers 2017, American Society of Civil Engineers, Orlando, Florida, United States, 766–772.

Yamamoto, K., Terao, Y., Fujii, T., Ikawa, T., Seki, M., Matsuzawa, M., Kanno, T., 2014. Operational overview of the first offshore production test of methane hydrates in the Eastern Nankai Trough, in: Offshore Technology Conference. Houston, Texas, United States.

Yang, L., Liu, Y., Zhang, H., Xiao, B., Guo, X., Wei, R., Xu, L., Sun, L., Yu, B., Leng,

S., Li, Y., 2019. The status of exploitation techniques of natural gas hydrate. Chin. J. Chem. Eng. 27(9), 2133–2147.

Yang, Y., Wang, K., Zhang, L., Sun, H., Zhang, K., Ma, J., 2019. Pore-scale simulation of shale oil flow based on pore network model. Fuel 251, 683–692.

Ye, J., Qin, X., Xie, W., Lu, H., Ma, B., Qiu, H., Liang, J., Lu, J., Kuang, Z., Lu, C., 2020. Main progress of the second gas hydrate trial production in the South China Sea. Geol. China 47(3), 557-568 (In Chinese with English abstract).

Yin, Z., Praveen, L., Praveen, Linga, 2019. Methane hydrates: A future clean energy resource. Chin. J. Chem. Eng. 27(9), 36–46.

You, K., Flemings, P.B., Malinverno, A., Collett, T.S., Darnell, K., 2019. Mechanisms of methane hydrate formation in geological systems. Rev. Geophys. 57(4), 1146–1196.

Yousif, M.H., Abass, H.H., Selim, M.S., Sloan, E.D., 1991. Experimental and theoretical investigation of methane-gas-hydrate dissociation in porous media. SPE reserve. Eng. 6(1), 69–76.

Zhang, L., Ge, K., Wang, J., Zhao, J., Song, Y., 2020. Pore-scale investigation of permeability evolution during hydrate formation using a pore network model based on X-ray CT. Mar. Pet. Geol. 113, 104157.

Zhang, Y., Liu, L., Wang, D., Zhang, Z., Li, C., Meng, Q., Liu, C., 2021a. The interface evolution during methane hydrate dissociation within quartz sands and its implications to the permeability prediction based on NMR data. Mar. Pet. Geol.

105065.

Zhang, Y., Wan, Y., Liu, L., Wang, D., Li, C., Liu, C., Wu, N., 2021b. Changes in reaction surface during the methane hydrate dissociation and its implications for hydrate production. Energy 230, 120848.

Zhao, J., Qin, F., Kang, Q., Qin, C., Derome, D., Carmeliet, J., 2022. A dynamic pore network model for imbibition simulation considering corner film flow. Water Resour. Res. 58, e2022WR032332.